Spring 1-1-2014

Computational Modeling of Unsteady Loads in Tidal Boundary Layers

Spencer R. Alexander
University of Colorado Boulder, antispencer@gmail.com

Computational modeling of unsteady loads in tidal boundary layers

by

Spencer R. Alexander

B.S., Rice University, 2008

A thesis submitted to the

Faculty of the Graduate School of the

University of Colorado in partial fulfillment

of the requirements for the degree of

Masters of Science

Department of Mechanical Engineering

2014

This thesis entitled:
Computational modeling of unsteady loads in tidal boundary layers
written by Spencer R. Alexander
has been approved for the Department of Mechanical Engineering

Dr. Peter Hamlington

Dr. Oleg Vasilyev

Dr. Daven Henzie

Date

The final copy of this thesis has been examined by the signatories, and we find that both the content and the form meet acceptable presentation standards of scholarly work in the above mentioned discipline.

Alexander, Spencer R. (M.S., Mechanical Engineering)

Computational modeling of unsteady loads in tidal boundary layers

Thesis directed by Dr. Peter Hamlington

As ocean current turbines move from the design stage into production and installation, a better understanding of oceanic turbulent flows and localized loading is required to more accurately predict turbine performance and durability. In the present study, large eddy simulations (LES) are used to measure the unsteady loads and bending moments that would be experienced by an ocean current turbine placed in a tidal channel. The LES model captures currents due to winds, waves, thermal convection, and tides, thereby providing a high degree of physical realism. Probability density functions, means, and variances of unsteady loads are calculated, and further statistical measures of the turbulent environment are also examined, including vertical profiles of Reynolds stresses, two-point correlations, and velocity structure functions. The simulations show that waves and tidal velocity had the largest impact on the strength of off-axis turbine loads. By contrast, boundary layer stability and wind speeds were shown to have minimal impact on the strength of off-axis turbine loads. It is shown both analytically and using simulation results that either transverse velocity structure functions or two-point transverse velocity spatial correlations are good predictors of unsteady loading in tidal channels.

Acknowledgements

I would like to begin by thanking Peter Hamlington for the two years of guidance and assistance. Helpful discussions with Drs. Peter Sullivan, Baylor Fox-Kemper, Jim Thomson, and Katherine McCaffrey are gratefully acknowledged. This work utilized the Janus supercomputer, which is supported by NSF (award number CNS-0821794) and the University of Colorado at Boulder. The Janus supercomputer is a joint effort of the University of Colorado at Boulder, the University of Colorado Denver and the National Center for Atmospheric Research.

Contents

Tables

Table

Figures

Figure

Chapter 1

Introduction

Deployments of renewable energy systems – including wind turbines, solar thermal collectors, hydroelectric dams, and many other technologies – have grown at a considerable pace over the past decade, and from 2005 to 2011 renewable energy capacity in the US increased by 300%[33]. In order to sustain this rapid increase, however, additional deployments and new sources of renewable energy are needed. Energy from the ocean has shown considerable promise as a predictable, abundant, and ideally-located resource, and it is estimated that ocean energy – comprising wave, tidal, current, and thermal energy – is capable of contributing an additional 400 TWh/yr, or 10% of the current US energy needs, to the US energy portfolio [33].

In order to increase the feasibility of large-scale ocean energy installations, further research is required to understand the turbulent oceanic environments in which ocean energy devices operate. Unsteady stresses and loads on ocean current turbines, in particular, are not well understood and may contribute to unexpectedly short turbine lifetimes due to gearbox and other component failures. Although ocean current turbines can be placed in open water far from coasts, tidal channels have long been seen as the most viable locations for such turbines due to the strong and highly predictable nature of tidal currents. The flow in tidal channels is, however, typically highly turbulent due to turbulence production by surface (i.e., wind) and bottom (i.e, no-slip) shears, waves, variable bathymetry (or bottom boundary surface roughness), thermal instabilities, and even turbines themselves (i.e., if a turbine is in the wake of another turbine). Turbulence from all of these sources can create substantial small-scale temporal and spatial variability of the tidal flow

field, resulting in potentially large off-axis and unsteady turbine loads.

In order to predict unsteady loads in such turbulent environments, simultaneous two-point spatial measurements are required across and downstream of the rotor disc. Observational data for such two-point statistics is, however, not yet available in tidal channels over the range of spatial scales (i.e., from meters to hundreds of meters) relevant to tidal turbine arrays. High fidelity computer simulations, by contrast, allow comparatively straightforward measurements of two-point statistics over a broad range of scales. Using simulations, the turbulent environments in which tidal current devices operate can be modeled, thereby enabling predictions of long-term turbine performance and unsteady fatigue loading.

Much of the current computational knowledge of tidal current loading is based on experience gained from studies of wind turbines, where attempts have been made to understand atmospheric turbulent environments and to assess the effects of bending moments on turbines. The interaction between the atmospheric boundary layer and utility scale wind turbines have been studied and classified using large-eddy simulations (LES), weather forecasting models and experiments. Calaf, Meneveau, and Meyers [4, 23, 24] developed an LES model to simulate an infinite wind farm and studied the characteristics of momentum entrainment. Churchfield **et al.** [7] simulated the Lillgrund offshore wind farm, both with and without turbines, with a particular focus on understanding turbulent wake characteristics. Lavely **et al.** [17] have shown that bending moments obtained using TurbSim [10] compare well to bending moments obtained from higher fidelity LES. Chamorro and Porté-Agel [5] have collected experimental data from a reduced-size wind turbine in a wind tunnel, and Porté-Agel **et al.** [29] have shown that the experimental measurements are reproduced with reasonable accuracy by LES. Kelley **et al.** [14] have examined the impact of coherent turbulence on the dynamic response and bending moments of wind turbines using both TurbSim and the Fatigue, Aerodynamics, Structures, and Turbulence (FAST) code [11], showing that the highest loads occur in stable, nighttime conditions.

Turbine loading and performance in the ocean have also been simulated, often with a strong focus on accurately modeling boundaries such as channel bathymetry and turbine blade shape.

Myers and Bahaj [26, 27, 3] have used blade element momentum (BEM) theory to understand wake and stress characteristics of horizontal axis marine current turbines, and McSherry **et al.** [21] and Malki **et al.** [19] both simulated the experimental setup of Bahaj **et al.** [2]. Churchfield **et al.** [6] have performed LES of an ocean current turbine in a tidal channel, comparing several the mean power output of several array configurations. Kang **et al.** [12, 13] have performed two studies related to marine current turbines, focusing heavily on the near-field flow behavior on turbine loads and torques; the simulations modeled bathymetry and turbine blades using curvilinear immersed boundaries. Afgan **et al.** [1] have performed a similar study of loading on a tidal stream turbine using LES.

By contrast to these prior studies, the present paper is focused on understanding the unsteady loads that would be experienced by a tidal current turbine in a realistic ocean environment, as well as how the loads correlate with fundamental turbulence statistics. These correlations are critical for predicting loads and, ultimately, turbine performance and fatigue in advance of installation. In order to resolve small-scale turbulent motions and increase the level of physical realism, LES has been performed of the ocean boundary layer for a range of different physical scenarios. Two of the scenarios are intended to simulate, as closely as possible, prospective tidal energy sites at Admiralty Head and Nodule Point in Puget Sound. LES results for these two locations are compared with observational measurements of the average velocity and turbulence intensity profiles from Thomson **et al.** [32]. The observational measurements have been used previously to examine turbulence intermittency, coherence, and anisotropy [20] and are used here to constrain the physical parameters used in the simulations, as well as to gain confidence in the accuracy of the LES.

A number of simulations for different physical scenarios have been performed in order to understand the effects of winds, waves, tidal velocity, stability, and tidal channel depth on the loads that would be experienced by a tidal turbine. Changes to the wind and tidal velocities result in changes to turbulence shear production, waves generate Langmuir turbulence [16, 22] which increases vertical mixing near the surface, and boundary layer stability strongly affects the creation and properties of convective turbulence. The LES model used in the present study has

the capability to model all of these effects and has been used previously for several high-fidelity process studies of atmospheric and oceanic flows[25, 22, 34, 9]. Probability density functions, two-point correlations, velocity structure functions, Reynolds stresses, and other statistics are used to understand the dependence of unsteady loads on each of these physical effects, and a connection is made between loads and two-point turbulence statistics.

It should be noted that the present study is differentiated from prior research by the extent of ocean physics included in the simulations and the focus on loads that would be experienced by a tidal current turbine. Prior studies have often neglected the effects of wind, waves, or tidal motions in order to decrease computational cost or to focus on impacts from other physical processes. In perhaps the most comprehensive prior study of tidal flows, Li **et al.** [18] studied temporally-varying tidal currents in an estuarine boundary layer, but did not consider waves, different stability conditions, or varying tidal channel depth, and were not specifically focused on tidal turbine loading. It should also be noted that the present study does not model turbines themselves. Rather, an attempt is made to understand how the loads that would be experienced by a tidal turbine are affected by different physical characteristics of the flow field in the tidal channel.

Chapter 2

Bending Moments and Loads

Quantification of the expected loads on a turbine in realistic ocean environments is an important objective of the present study. Prior research has been performed on wind turbine loading for different atmospheric conditions [14, 11, 28, 15], including the specific loading associated with the blade structure. Similar computational and experimental studies have been performed on loads experienced by ocean current turbines [2, 26, 27, 3, 21, 19, 6, 12, 13, 1], but the dependence of such loads on characteristics of the oceanic boundary layer such as wind and wave shear, boundary layer depth, and stability conditions have yet to be performed.

In the present paper, the loads that would be experienced by a tidal turbine are considered, without restricting the analysis to a specific choice of turbine design. The loads at location $[x, y, z]$, denoted $M_i(x, y, z)$, are thus measured for a rigid, infinitesimally thin disc and are calculated by an integral over the area of the disc as

$$M_i(x, y, z, t) = \int_A \rho \epsilon_{ijk} r_j u_k u_x dA \,, \tag{2.1}$$

where ϵ_{ijk} is the cyclic permutation tensor, $r_j = [r_x, r_y, r_z]$ is the distance from the central point to a location on the disc, u_x is the velocity normal to the disc, $u_k = [u_x, u_y, u_z]$, and A is the cross-sectional area of the disc. The velocities in this relation are evaluated at each location on the disc, given by the vector $(x_i + r_i)$, where $x_i = [x, y, z]$. Since the disc is assumed to be infinitely

thin, $r_x = 0$ and (2.1) can be expanded as

$$M_x(x,y,z,t) = \int_A \rho(r_y u_z - r_z u_y) u_x dA\,, \tag{2.2}$$

$$M_y(x,y,z,t) = \int_A \rho r_z u_x^2 dA\,, \tag{2.3}$$

$$M_z(x,y,z,t) = -\int_A \rho r_y u_x^2 dA\,. \tag{2.4}$$

The component M_x is about the axis normal to the turbine disk and provides a torque that either accelerates or decelerates the turbine. The components M_y and M_z are bending moments about the horizontal and vertical bisects of the turbine disk, respectively (see Figure 2.1), and are termed in the following **off-axis** loads.

2.1 Relation to Turbulence Characteristics

The primary focus in this study is on the off-axis bending moments and loads, M_y and M_z, which are related to the characteristics of the turbulent flow field. It can be anticipated that the relevant turbulence characteristics are related to transverse velocity differences over different spatial separations across the rotor disc. This can be shown explicitly by first noting that the integrals for M_y and M_z in (2.3) and (2.4) can be equivalently written as

$$M_y(x,y,z) = \int_{r_y}\int_{r_z} \rho r_z \left[u_x^2(x,y,z+r_z) - u_x^2(x,y,z-r_z)\right] dr_z dr_y, \tag{2.5}$$

$$M_z(x,y,z) = -\int_{r_z}\int_{r_y} \rho r_y \left[u_x^2(x,y+r_y,z) - u_x^2(x,y-r_y,z)\right] dr_y dr_z, \tag{2.6}$$

where the bounds of the integrals are determined by the specific shape and size of the rotor disc and the time coordinate t has been suppressed to simplify the notation. The outer integrals in (2.5) and (2.6) simply accumulate the moments about the y and z axes, respectively, and for the purposes of the analysis it is informative to consider only the inner integrals. These integrals are denoted m_y and m_z and are given as

$$m_y(x,y,z) = \int_0^{a_z} \rho r_z \left(\Delta_{r_z} u_x\right) \left[u_x(x,y,z+r_z) + u_x(x,y,z-r_z)\right] dr_z\,, \tag{2.7}$$

$$m_z(x,y,z) = -\int_0^{a_y} \rho r_y \left(\Delta_{r_y} u_x\right) \left[u_x(x,y+r_y,z) + u_x(x,y-r_y,z)\right] dr_y\,, \tag{2.8}$$

where a_y and a_z are the dimensions of the rotor diss along the y and z axes, respectively, and the transverse velocity differences

$$\Delta_{r_z} u_x \equiv u_x(x, y, z + r_z) - u_x(x, y, z - r_z)\,, \tag{2.9}$$

$$\Delta_{r_y} u_x \equiv u_x(x, y + r_y, z) - u_x(x, y - r_y, z)\,, \tag{2.10}$$

have been introduced. Using the Reynolds stress decomposition $u_i = u_i' + \overline{u}_i(z)$, where $\overline{(\cdot)}$ is a time or ensemble average, it is possible to rewrite m_y and m_z as

$$m_y(x, y, z) \approx 2\rho\overline{u}_x \left[\int_0^{a_z} r_z \left(\Delta_{r_z} u_x'\right) dr_z + \int_0^{a_z} r_z \left(\Delta_{r_z} \overline{u}_x\right) dr_z\right], \tag{2.11}$$

$$m_z(x, y, z) \approx -2\rho\overline{u}_x \int_0^{a_y} r_y \left(\Delta_{r_y} u_x'\right) dr_y\,, \tag{2.12}$$

where it is assumed that ρ is approximately constant (a safe approximation in reality and in the context of the Boussinesq equations that are solved in the present simulations), that $\overline{u}_x(z) \approx [\overline{u}_x(z + r_z) + \overline{u}_x(z - r_z)]/2$, and that $|\overline{u}_x|$ is much greater than $|u_x'|$ (typically the latter is only 10% of the former). These are the only approximations used in the analysis outlined here.

In (2.11), there is a persistent contribution to m_y from the mean shear. In order to consider only the turbulent parts of m_y and m_z, the fluctuating moments can be separately written as $m_y' = m_y - \overline{m}_y$ and $m_z' = m_z - \overline{m}_z$, giving

$$m_y' \approx 2\rho\overline{u}_x T_{zx}' \quad \text{and} \quad m_z' \approx -2\rho\overline{u}_x T_{yx}'\,, \tag{2.13}$$

where

$$T_{ix}' \equiv \int_0^{a_i} r_i \left(\Delta_{r_i} u_x'\right) dr_i\,, \tag{2.14}$$

and $\overline{m}_z = 0$. The corresponding average magnitudes of m_y' and m_z' are then given by

$$\overline{|m_y'|} \approx 2\rho\overline{u}_x \overline{|T_{zx}'|} \quad \text{and} \quad \overline{|m_z'|} \approx -2\rho\overline{u}_x \overline{|T_{yx}'|}\,, \tag{2.15}$$

where $\overline{u}_x$ is assumed positive. The statistics $\overline{|T_{zx}'|}$ and $\overline{|T_{yx}'|}$ represent the key turbulence metrics for determining unsteady bending moments. Neither of these quantities are, however, standard

turbulence statistics, and we can obtain upper bounds on the average magnitudes of m'_y and m'_z in terms of a more conventional turbulence statistic using the triangle inequality, which gives

$$\overline{|m'_y|} \lesssim 2\rho\overline{u}_x \int_0^{a_z} r_z \overline{|\Delta_{r_z} u'_x|} dr_z \,, \tag{2.16}$$

$$\overline{|m'_z|} \lesssim 2\rho\overline{u}_x \int_0^{a_y} r_y \overline{|\Delta_{r_y} u'_x|} dr_y \,. \tag{2.17}$$

These relations indicate that the first order transverse velocity structure function provides an upper bound on the moments experienced by a turbine. The structure function is weighted by the separation r_z or r_y and integrated in order to obtain the average turbulent bending moment magnitudes. In the following, the correlation of the off-axis bending moments with the transverse velocity structure functions will be examined for a range of oceanic conditions.

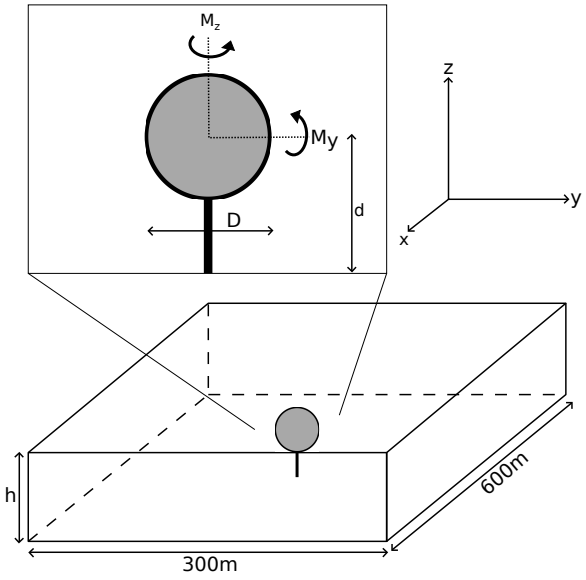

Figure 2.1: Schematic showing the computational domain used in the simulations and the infinitely thin disc about which the off-axis bending moments M_y and M_z are calculated. The disc diameter is D and the hub height is denoted d.

Chapter 3

Details of the Numerical Simulations

In order to represent the effects of winds, waves, and tides, the numerical simulations solve the forced Wave-Averaged Boussinesq (WAB) equations given by

$$\frac{\partial \mathbf{u}}{\partial t} + \boldsymbol{\omega} \times \mathbf{u}_L = -\nabla \left(p + \frac{1}{2}|\mathbf{u}_L|^2 \right) + \boldsymbol{b} + \mathbf{F}_c + sgs, \tag{3.1}$$

$$\frac{\partial \theta}{\partial t} + \mathbf{u}_L \cdot \nabla \theta = sgs, \tag{3.2}$$

$$\nabla \cdot \mathbf{u} = 0, \tag{3.3}$$

where $\mathbf{u}$ is the three-dimensional Eulerian flow velocity, $\boldsymbol{\omega} \equiv \nabla \times \mathbf{u}$ is the Eulerian vorticity, $\mathbf{u}_L = \mathbf{u} + \mathbf{u}_s$ is the Lagrangian velocity, $\mathbf{u}_s$ is the wave-induced Stokes drift velocity, p is the pressure normalized by the background density ρ_0, $\mathbf{b}$ is the buoyancy, $\mathbf{F}_c$ is a driving term used to create the tidal current, θ is the potential temperature, and sgs represents subgrid-scale (sgs) terms introduced by the LES modeling. Note that in the present study Coriolis effects are not considered; a similar approach has been used in prior studies of tidal boundary layers [18] and rotational effects are not expected to have a significant contribution to the dynamics at the range of scales examined here. Closure of the governing equations is achieved by introducing an equation of state for the density ρ, namely

$$\rho = \rho_0 \left[1 + \beta_T (\theta_0 - \theta) \right], \tag{3.4}$$

where $\beta = 2 \times 10^{-4} \mathrm{K}^{-1}$ is the thermal expansion coefficient and salinity effects have been neglected. The buoyancy is then obtained as $\mathbf{b} = b\hat{\mathbf{z}}$ where $b = -g\rho/\rho_0$. Parameter values used to obtain the buoyancy are $\rho_0 = 1000 \mathrm{kg/m}^3$, $\theta_0 = 290.16 \mathrm{K}$ and $g = 9.81 \mathrm{m/s}^2$.

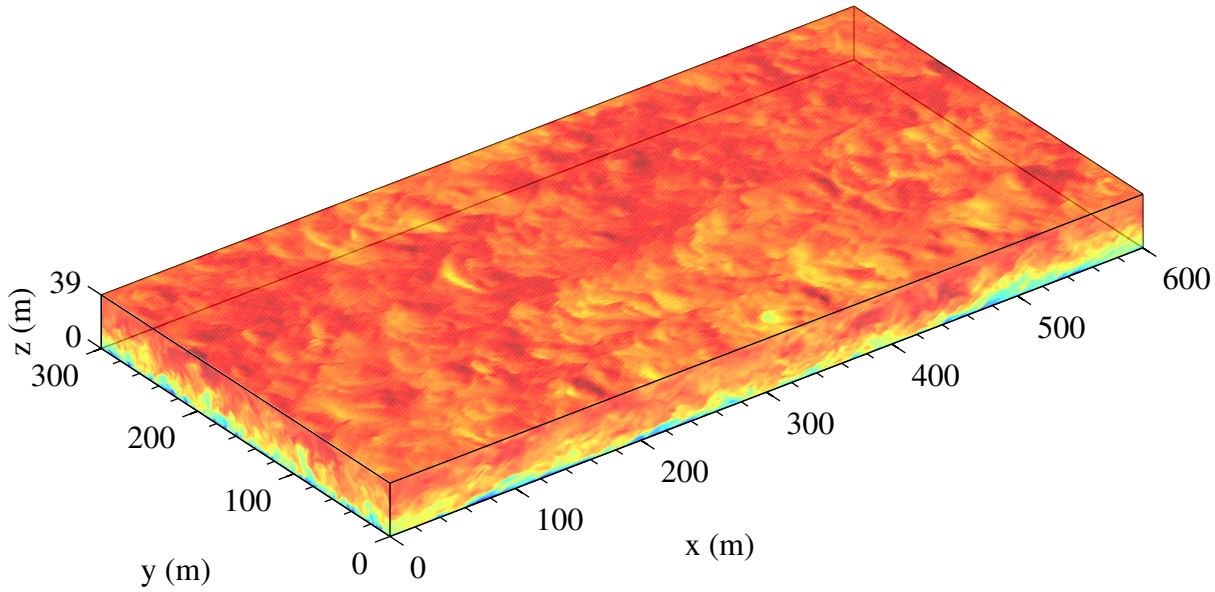

Figure 3.1: 3d volume snapshot of u_x for the B simulation

The simulations are fully periodic in the horizontal $(x - y)$ directions for all simulation variables. This results in an inflow that is directly tied to the outflow. On the top boundary, the horizontal velocities are driven by a wind shear stress u_τ in the ϑ_s direction – in these simulations, ϑ_s is always chosen to be in the positive x direction, resulting in a wind shear stress of u_τ in the x direction and no shear stress in the y direction. The vertical velocity constrained to zero at the top boundary. Depending on the stability of the simulations, either a cooling, warming, or adiabatic boundary condition temperature flux, Q_0, is applied at the top boundary. At the bottom boundary, a no-slip condition is used for velocities in all three directions, and the temperature flux is zero. The surface roughness for the bottom no-slip boundary is $z_0 = 0.001$m, and the SGS model used in the LES matches the log-law for the mean velocity at the lower boundary (as described in Sullivan **et al.** [30]).

The WAB equations, which have been used previously in a number of computational studies of wave-driven Langmuir turbulence [22, 34, 9], are a wave-averaged form of the standard Boussinesq equations and include the effects of wave forcing via the Stokes drift velocity $\mathbf{u}_s$. The Stokes drift

velocity is modeled as

$$\mathbf{u}_s = u_s(z)\left[\cos(\vartheta_s)\hat{\mathbf{x}} + \sin(\vartheta_s)\hat{\mathbf{y}}\right] , \tag{3.5}$$

where $u_s(z)$ is the Stokes drift velocity vertical profile and ϑ_s is the wave direction. Using the Donelan empirical spectrum [8, 35] for the ocean wave field, the resulting vertical profile $u_s(z)$ decreases super-exponentially with depth. In the simulations, the Stokes drift velocity is assumed to be the same at all horizontal $(x-y)$ locations with an angle of $\vartheta_s = 0°$. That is, the wave field is assumed to be perfectly aligned with the mean tidal direction (see the schematic in Figure 2.1). The magnitude of the Stokes drift is determined by assuming a 10m wind speed, U_{10}, between 0m/s and 10m/s, resulting in a surface Stokes drift of 0.063m/s and a turbulent Langmuir number $La_t = \sqrt{u_\tau/u_s(0)} = 0.29$, where $u_\tau = 0.0061$m/s is the top wind shear friction velocity.

The WAB equations with the Stokes drift given by (3.5) lead to the creation of near surface Langmuir turbulence in the simulations [22, 34, 9]. Langmuir turbulence consists of disordered collections of counter-rotating vortical cells (typically called 'Langmuir' cells). These cells are typically 10m deep in the vertical and up to 1km long in the horizontal direction. They create surface convergence zones where foam, plankton, and other debris collect, resulting in characteristic 'windrows.' The primary effect of Langmuir turbulence on the flow field is to create more intense vertical mixing, which may substantially alter the loads experienced by a turbine in a tidal channel.

The forcing term, $\mathbf{F}_p = F_p\hat{\mathbf{x}}$, in (3.1) creates the tidal current and is constant in both space and time; following Li **et al.** [18], future work will vary F_p in order to consider situations in which the tidal stream changes magnitude and direction. The strength of F_p is adjusted in order to create the desired tidal velocity, which varied from 1m/s to 3m/s in the present simulations.

The SGS model used in the simulations was described by Sullivan **et al.** [30], and takes into account not only sub-grid influences proportional to the resolved-scale strain rate S_{ij}, but also influences proportional to the horizontal average strain rate, $\overline{S}_{ij}$, namely

$$\tau_{ij} = 2\nu_t\gamma S_{ij} - 2\nu_T\overline{S}_{ij} , \tag{3.6}$$

where τ_{ij} are the SGS stresses, ν_t and ν_T are eddy viscosities, and γ is an isotropy factor. The

Smagorinsky model is used to write ν_t as

$$\nu_t = (C_s\Delta)^2\sqrt{2S_{ij}S_{ij}}\,, \quad C_s = \left(C_k\sqrt{\frac{C_k}{C_e}}\right)^{1/2}\,, \tag{3.7}$$

and the mean flow eddy viscosity, ν_T, is given by

$$\nu_T = (C_K L_m)^2\sqrt{\left(\frac{\partial\overline{u}_x}{\partial z}\right)^2 + \left(\frac{\partial\overline{u}_y}{\partial z}\right)^2}\,, \tag{3.8}$$

where u_x and u_y are horizontal velocities in the streamwise and transverse directions, respectively. The model coefficients are $C_k = 0.1$, $C_e = 0.93$, and the product $C_K L_m$ is chosen to match Monin-Obukhov similarity theory near the bottom boundary [30]. The isotropy factor, γ, is given in terms of the strain rate magnitudes $S' \equiv \sqrt{2\overline{S'^2}_{ij}}$ and $S \equiv \sqrt{2\overline{S}^2_{ij}}$ as

$$\gamma = \frac{S'}{S' + \overline{S}}\,, \tag{3.9}$$

where $S'_{ij} \equiv S_{ij} - \overline{S}_{ij}$. The additional influence of horizontal average strain rates introduced by the $2\nu_T\overline{S}_{ij}$ term in the expression for τ_{ij} improves the agreement of vertical velocity and temperature profiles with Monin-Obukhov theory.

The National Center for Atmospheric Research (NCAR) LES model has been used to perform the simulations [25, 22]. The code solves the WAB equations on a structured, rectilinear grid. A spectral method is used in horizontal directions and a second-order finite difference method is used in the vertical direction for the velocities. A second-order finite difference method is used in the vertical direction for scalar variables such as the potential temperature. A three-step explicit Runge-Kutta method is used to advance the solution in time, and the Poisson pressure equation is solved iteratively at each time step.

The physical setup and conditions used in the numerical simulations were chosen to represent wind-, wave-, and tidally-driven ocean boundary layers that approximately correspond to those found at Admiralty Head and Nodule Point in Puget Sound. These sites have been characterized in Thomson **et al.** [32] and recently-collected data allows comparisons to be made between the simulation and experimental results, thereby providing an assessment of the simulation accuracy.

Since the present simulations are, however, more broadly focused on the effects of winds, waves, boundary layer depth, instabilities, and tidal velocity, a series of 13 simulations corresponding to 11 different physical scenarios have been performed, as summarized in Table 3.1. The baseline simulation (denoted 'B' in Table 3.1) has horizontal lengths $L_x = 600$m and $L_y = 300$m with depth $H = 39$m, a tidal velocity of $U_t = 2$m/s, upper wind forcing resulting in $u_\tau = 6.3$mm/s, waves, and no heat flux at the surface (corresponding to a neutral boundary layer). All other simulations have identical L_x and L_y to the baseline case, but H is varied to 22m and 56m in two of the simulations (denoted H_- and H_+ in Table 3.1). Similarly, the tidal velocity (T_- and T_+), wind strength (Wi_- and Wi_+), wave strength (Wa_- and Wa_+), and surface heat flux (In_- and In_+) are each varied to be successively smaller and larger than the baseline values, resulting in a series of simulations that allow each of these effects to be individually measured. A final pair of simulations with identical physical parameters to the baseline simulation but with doubled (B_+) and halved (B_-) resolution are performed in order to ascertain grid convergence.

Table 3.1: Summary of the physical setup used in each of the simulations. Horizontal and vertical physical domain sizes are denoted L_x, L_y, and h, computational domain sizes are given by N_x, N_y, and N_z, U_t is the tidal velocity, u_τ is the surface friction velocity, τ is the wind stress, ϑ_w is the wind direction with respect to the x-axis, $u_s(0)$ is the Stokes drift velocity at the surface, $La_t = u_\tau/u_s(0)$ is the turbulent Langmuir number, ϑ_s is the Stokes drift direction with respect to the x-axis, and Q_0 is the surface heat flux. Parameters varied in each of the simulations are shown in bold.

Simulation	B	B_-	B_+	Wi_-	Wi_+	Wa_-	Wa_+	H_-	H_+	In_-	In_+	T_-	T_+
L_x (m)	600	600	600	600	600	600	600	600	600	600	600	600	600
L_y (m)	300	300	300	300	300	300	300	300	300	300	300	300	300
h (m)	39	39	39	39	39	39	39	**22**	**56**	39	39	39	39
N_x	512	**256**	**1024**	512	512	512	512	512	512	512	512	512	512
N_y	256	**128**	**512**	256	256	256	256	256	256	256	256	256	256
N_z	128	**64**	**256**	128	128	128	128	**72**	**184**	128	128	128	128
U_t (m/s)	2.0	2.0	2.0	2.0	2.0	2.0	2.0	2.0	2.0	2.0	2.0	**1.0**	**3.0**
u_τ (mm/s)	6.3	6.3	6.3	**0.0**	**12.6**	6.3	6.3	6.3	6.3	6.3	6.3	6.3	6.3
τ (N/m^2)	0.04	0.04	0.04	**0.00**	**0.08**	0.04	0.04	0.04	0.04	0.04	0.04	0.04	0.04
ϑ_w (°)	0	0	0	0	0	0	0	0	0	0	0	0	0
$u_s(0)$ (m/s)	0.099	0.099	0.099	0.099	0.099	**0**	**0.20**	0.099	0.099	0.099	0.099	0.099	0.099
La_t	0.25	0.25	0.25	**0.0**	**0.35**	∞	**0.18**	0.25	0.25	0.25	0.25	0.25	0.25
ϑ_s (°)	0	0	0	0	0	0	0	0	0	0	0	0	0
Q_0 (W/m^2)	0	0	0	0	0	0	0	0	0	**-5.0**	**5.0**	0	0
z_0 (m)	10^{-3}	10^{-3}	10^{-3}	10^{-3}	10^{-3}	10^{-3}	10^{-3}	10^{-3}	10^{-3}	10^{-3}	10^{-3}	10^{-3}	10^{-3}

Chapter 4

Results

After an initial spin-up period during which the boundary layer turbulence was allowed to develop, each of the simulations summarized in Table 3.1 were run for a total of six hours of virtual time, with an average timestep of 0.15 seconds for simulations of base resolution. Higher resolution simulations (i.e., B_+) had smaller average timesteps and more overall timesteps. The simulated time was sufficient to allow turbulence to fully develop, and the u_x velocity and Reynolds stress profiles were stable and unchanging with additional simulation time.

In the following, a validation of the simulation results is outlined, including a study of grid convergence. Single-point statistics of the velocity and temperature for the different simulations are then presented, followed by an analysis of two point turbulence statistics. Finally, off-axis loads for each of the different physical scenarios summarized in Table 3.1 are outlined.

4.1 Validation and Grid Convergence

Validation of the physical parameters and numerical methods is critical for grounding simulations in reality and identifying lingering numerical issues. Validation of the simulations is performed through comparison with theory, prior studies, and observational data from Thomson **et al.** [32]. Prior work by Sullivan and Patton in the atmospheric convective boundary layer [31] indicate that mesh sizes of 256^3 were sufficient for achieving scale separation between the large energy containing eddies and the filter cutoff scale, and this study was the starting point for our mesh resolution choices – below these choices are validated by comparing statistics from three mesh resolution

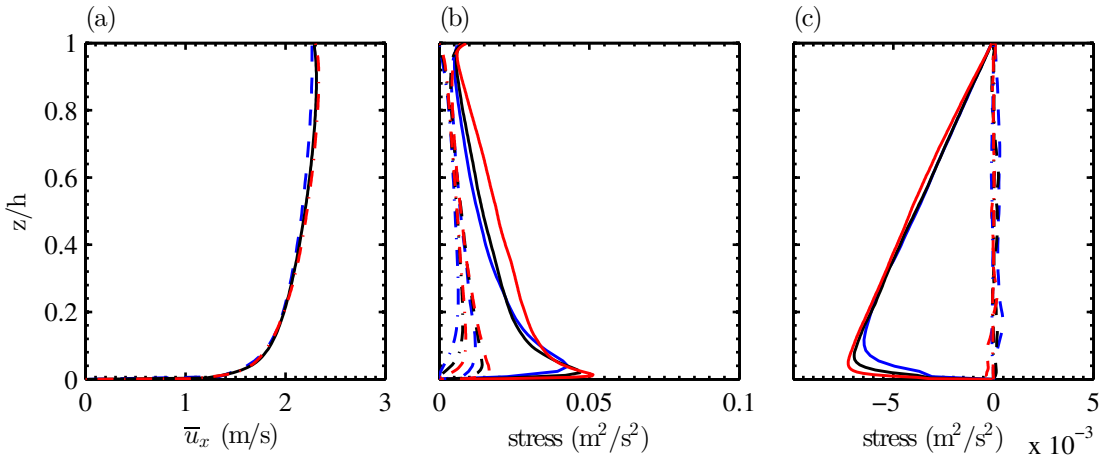

Figure 4.1: Vertical profiles of (a) $\bar{u}_x$, (b) diagonal Reynolds stresses, $\overline{u_x'^2}$ (solid), $\overline{u_y'^2}$ (dashed) and $\overline{u_z'^2}$ (dash-dot), and (c) off-diagonal Reynolds stresses, $\overline{u_x'u_z'}$ (solid), $\overline{u_x'u_y'}$ (dashed), $\overline{u_y'u_z'}$ (dash-dot). Each plot showing values for three different grid resolutions, corresponding to the simulations B (solid black lines), B$_-$ (blue dashed lines), and B$_+$ (red dash-dot lines), as a function of z/h.

studies.

Figure 4.1 shows vertical profiles of u_x along with diagonal and off-diagonal Reynolds stresses for the B, B$_-$ and B$_+$ simulations. The profile of u_x shows good agreement with the theoretically-predicted log-layer profile and the qualitative behavior of the diagonal and off-diagonal Reynolds stresses is consistent with prior studies of wall bounded shear flows. That is, $\overline{u_x'^2} > \overline{u_y'^2} > \overline{u_z'^2}$ and $\overline{u_x'u_z'} < 0$, with the greatest magnitudes of all stresses occurring close to the bottom boundary at $z \approx 0$. The vertical Reynolds stress profiles also show good agreement with previous studies of the atmosphere [25, 31] and tidal channels [6].

From a more quantitative perspective, deviations of the simulation results from the theoretical log-layer profile are characterized by the quantity ϕ_m, which is defined as [30, 6]

$$\phi_m(z) \equiv \frac{\kappa z}{u_*}\frac{\partial U_s}{\partial z}\,, \tag{4.1}$$

where $U_S \equiv [\overline{u_X} + \overline{u_y}]^{1/2}$, $\kappa = 0.41$, and u_* is the friction velocity. While the ϕ_m profile for the B simulation, shown in Figure 4.2, is not precisely unity, as would be expected in the case of a perfect log-layer profile, the small deviations are consistent with previous studies of atmospheric and oceanic boundary layers [30, 6]. The deviations are largest near the channel bottom, approaching

a high value of 1.2 and a low value of 0.7. In the simulations, grid anisotropy (i.e., the ratio of Δx to Δz) was found to have a large effect on the ϕ_m profile, with higher values of the ratio (> 10) resulting in more substantial deviations from unity. Decreasing the grid anisotropy to a ratio below four brought the ϕ_m profiles shown in Figure 4.2 in line with previous studies[30, 6].

Comparisons with the observational data of Thomson **et al.**[32] are made using the turbulence intensity (TI), which is defined as

$$\mathrm{TI} \equiv \frac{\overline{u_x'^2}^{1/2}}{\overline{u}_x} \,. \tag{4.2}$$

The resulting vertical profiles of TI are shown in Figure 4.3 for the simulations B (corresponding to a 39m depth), H_- (corresponding to a 22m depth at the Nodule Point location), and H_+ (corresponding to a 56m depth at the Admiralty Head location)[32]. Figure 4.3 shows that the simulations correctly capture the basic shape of the observational TI profiles, but slightly underestimate the magnitude of the TI (note that observational data were only available up to roughly 18m above the ocean bottom). The LES results for all depths show a large increase in TI near the bottom of the ocean boundary layer where u_x decreases to zero. While the physical parameters in the simulations were designed to match, as closely as possible, the roughness lengths inferred from the observations, increases in the roughness length above the observed length were found to increase the magnitude of the vertical profile of TI. It should also be noted that an increase in grid resolution (B_+) resulted in a slight (roughly 5%) increase in the magnitude of the TI profile. Nevertheless, the good qualitative agreement and approximate quantitative agreement between the LES results and observations shown in Figure 4.3 provides confidence in the validity of the simulations.

Finally, Figures 4.1 and 4.2 show the effects of varying grid resolution, corresponding to low (the B_- simulation), base (B), and high (B_+) resolutions, on the velocity and Reynolds stress profiles. The vertical profiles of u_x in Figure 4.1(a) show that there is good agreement between the base and high resolution runs, with slight deviations near the top of the boundary layer for the low resolution run. The diagonal Reynolds stresses in Figure 4.2(b) show moderate variations for the three runs along the entire depth of the domain, while the $\overline{u_x' u_z'}$ Reynolds stress in Figure 4.2(c)

shows good agreement for z/h between 0.2 and 1, with more substantial deviations in the lower resolution run. The ϕ_m profiles in Figure 4.2, show similar deviations from unity for all three resolutions, but the deviations occur at heights proportional to the grid size. In particular, the ϕ_m profile for the highest resolution run does not show substantially less deviation from unity, just a deviation at a height closer to $z/h = 0$.

Overall, the simulations with different grid resolutions indicate that the resolution of the base run (B) captures most statistics with acceptable accuracy relative to a simulation with grid resolution doubled in each direction. In the interest of exploring as large a parameter space as possible, the resolution of the base simulations appears to be appropriate for developing insights into the variation of off-axis loads for varying winds, waves, stability, and other physical parameters.

4.2 Single-Point Statistics

Single-point statistics are the current norm in understanding ocean current environments. The single point moments provide valuable information to developers, designers and simulators regarding mean flow levels, turbulence levels, and transient effects. However, their ability to predict bending moments and off-axis loading remains questionable. In this section, we describe the impact of various physical parameters on single-point statistics, and in sections 4.4 and 5 link these single-point statistics to bending moments.

Figures 4.4(a) and (c) show that profiles of the mean velocity $\overline{u}_x$ do not change substantially as either the wind or instability conditions change. Changes in the wave strength do, however, affect $\overline{u}_x$ near the surface, where $\overline{u}_x$ for Wa_+ decreases below the corresponding values for B and Wa_-, as shown in Figure 4.4(b). The increased wave strength for the Wa_+ simulation, modeled as a stronger Stokes drift velocity (see Table 3.1), results in an anti-Stokes effect, as previously observed in Hamlington **et al.**[9]. The profiles of $\overline{u}_x$ also change for T_- and T_+ as compared to the base case due to the large changes in mean tidal velocity. Overall, the general uniformity of the mean velocity profile with respect to changes in the wind, wave, and stability conditions is significant in the design of loads, since a drastic change in vertical velocity profile for different

physical parameters would result in added complexity towards addressing mean vertical shear.

The vertical profiles of Reynolds stress are shown in Figure 4.5 and provide insights into the level of turbulent activity within the flow. Both the Wa_+ and In_+ simulations show a substantial increase in $\overline{u_x'^2}$ compared to the base case, although little change is seen in either $\overline{u_z'^2}$ or $\overline{u_x' u_z'}$. This increase in $\overline{u_x'^2}$ represents a substantial increase in the largest component of turbulence kinetic energy, and will impact not only the bending loads discussed in this paper, but also transient torquing loads. Strong deviations from the base Reynolds stress profiles are present in the T_- and T_+ profiles, and the magnitudes of the changes is worth noting: a 50% increase of mean velocity approximately doubles the $\overline{u_x'^2}$ Reynolds stress, while halving the mean velocity results in roughly a factor of four decrease in $\overline{u_x'^2}$.

The mean temperature profiles remain close to the background value θ_0 for all simulations except the unstable (In_-) and stable (In_+) cases. Figure 4.6 shows that there is a sharp increase in the mean potential temperature $\overline{\theta - \theta_0}$ for In_+ due to heating at the surface while there is a sharp decrease for In_- due to surface cooling. These large changes in the temperature profiles are accompanied by corresponding changes in the temperature fluxes, as shown in Figure 4.7. For the unstable case (In_-), $\overline{u_x'\theta'} < 0$, corresponding to an anti-correlation between u_x' and θ', while for the stable case (In_+), $\overline{u_x'\theta'} > 0$. In Figure 4.7(c), $\overline{u_z'\theta'} > 0$ for the unstable case, corresponding to an upward flux of low temperatures as the surface is cooled, while $\overline{u_z'\theta'} < 0$ for the stable case, corresponding to a downward flux of high temperatures as the surface is heated. The horizontal fluxes in Figure 4.7(b) for the stable and unstable cases remain close to zero. It should be noted that there are large variations in $\overline{u_x'\theta'}$ and $\overline{u_y'\theta'}$ for the base case (B). These variations are due primarily to large $\overline{\theta'^2}$ in the base simulation resulting from no imposed constraint on the correlation between the horizontal turbulence velocities and θ', other than the condition that the vertical flux of θ' be zero at the surface.

4.3 Two-Point Statistics

Two-point velocity correlation functions and integral length scales have been shown in prior studies[14] to be accurate predictors of wind turbine loading. The bending moment analysis in Section 3 also indicates the importance of two-point statistics closely related to correlation functions in understanding and predicting off-axis turbine loads. Prior studies[14] have shown that when the integral length scale of the turbulence is similar to the diameter of the turbine rotor, the loads on the turbine are greatest – turbulence with this characteristic length scale results in large velocity gradients across the rotor swept area and corresponding high bending moments.

Figure 4.8 shows the longitudinal velocity correlation, f_{11}, and transverse velocity correlation, f_{12}, as functions of height, where

$$f_{11}(z,\Delta x) = \frac{\overline{u'_x(x,y,z)u'_x(x+\Delta x,y,z)}}{\overline{u'^2_x}}\,, \quad f_{12}(z,\Delta y) = \frac{\overline{u'_x(x,y,z)u'_x(x,y+\Delta y,z)}}{\overline{u'^2_x}}\,, \tag{4.3}$$

and the corresponding integral scales Λ_{11} and Λ_{12} are defined as

$$\Lambda_{11}(z) = \int_0^\infty f_{11}(z,x')dx'\,, \quad \Lambda_{12}(z) = \int_0^\infty f_{12}(z,y')dy'\,. \tag{4.4}$$

In the base case, the longitudinal length scale (i.e., the coordinate Δx) varies from 20-50m (2-5D for a 10m diameter turbine) and the transverse length scale (i.e., Δy) varies from 0-20m (0-2D for a 10m diameter turbine). Figure 4.8(a) shows that, generally, the turbulence remains longitudinally correlated for larger Δx as z/h increases, although the correlation approaches zero at the upper surface; these variations are reflected in the increase of $\Lambda_{11}(z)$ with increasing z/h. For the transverse correlation f_{12} in Figure 4.8(b), $\Lambda_{12}(z)$ increases monotonically with increasing z/h, reflecting increased transverse correlations for larger Δy from the bottom to the top of the tidal channel.

As shown in Figure 4.9, the transverse correlation f_{12}, which is of central importance in understanding off-axis loading, is qualitatively similar for all of the simulations performed in the present study. As in Figures 4.4 and 4.5 for the mean velocities and Reynolds stresses, respectively, the largest changes in f_{12} occur as the wave forcing varies, with approximately a factor of two

increase in Λ_{12} at all z/h for the Wa$_-$ simulation. This indicates that the greatest changes in bending moments may occur as the wave forcing is varied. The transverse length scale also varies for the other simulations, but magnitude changes are more modest, on the order of 10%.

In addition to understanding the scale of the turbulent fluxes present in the ocean boundary, it is also important to understand the magnitude and distribution of these velocity variations – these two properties feed directly into the distribution of bending moments experienced at the turbine level, as discussed in Section 2. To understand these spatial velocity differences, Figure 4.10 shows structure functions S_{1j}, defined as

$$S_{1j}(z, r_j) = \frac{\overline{|u'_x(\mathbf{x} + \mathbf{r}_j) - u'_x(\mathbf{x} - \mathbf{r}_j)|}}{\overline{u'^2_x}^{1/2}}, \tag{4.5}$$

where $\mathbf{x}$ is a position in space and $\mathbf{r}_j$ is a vector of length r_j in the x_j direction. Each of the structure functions shown in Figure 4.10 follow an approximate $r^{1/3}$ scaling, in accordance with classical Kolmogorov theory, although the departures from this scaling are greatest for S_{11} and S_{12} near the surface. In both cases, the structure functions have reduced slope, indicating greater prominence of large scale motions relative to small scales.

Finally, Figure 4.11 shows probability density functions (pdfs) of the transverse velocity increments $\Delta_{r_y} u_x$ for different values of Δ_{r_y}. In general, the pdfs become increasingly non-Gaussian as Δ_{r_y} decreases, and the pdfs for Δ_{r_y} at typical rotor radii ($\sim$5m) show indications of non-Gaussianity and intermittency. The implications of this are significant for models that assume a normal distribution of velocity differences, since Figure 4.11 shows that extreme events, leading to greater off-axis loads, will occur more frequently than expected from a normal distribution.

4.4 Bending Moments

The final component of the analysis regards bending moments, which are outlined analytically in Section 2. These bending moments are primary drivers of turbine design, and understanding the magnitude and physical properties of the moments will aid in designing and predicting performance of ocean current turbines. Two primary types of bending moments are considered here: shear-

dominated moments, M_y, and eddy-dominated moments, M_z. The eddy dominated moments are so named since they have zero means for the $x - y$ homogeneous tidal channels examined in the present study.

Figure 4.12(a) shows that M_y is strongly dominated by mean shear in the flow and increases substantially as z/h approaches zero where the mean shear is largest. The magnitude of the median bending moment at the channel bottom is three times larger than the median bending moment at the surface, with half of the change occurring in the bottom 10% of the ocean boundary. The 90th percentile bending moment is approximately double the median bending moment, and the two vertical profiles are qualitatively very similar.

Changes to the M_y bending moment for the different simulation cases, as shown in Figure 4.13, are subtle but important. In Figures 4.13 (a) and (b), both decreasing the waves and increasing the wind, which increases the turbulent Langmuir number (La_t), result in an overall decrease in M_y for all z levels. The effect of increasing the wave forcing (bottom row of Figure 4.13(b)) and increasing the turbulent Langmuir number is both more significant and more complex; M_y increases near the surface but decreases in the middle half of the boundary layer. This change is attributable to a similar change in the mean velocity profile, shown in Figure 4.4, where the increased wave forcing case was the only case to substantially change the mean velocity profile. Changes in stability have little impact on M_y and, as expected, the bending moments are very sensitive to changes in mean tidal velocity (Figure 4.13(d)).

The eddy dominated bending moments, M_z, shown in Figure 4.12(b), are driven by horizontal imbalances in downstream velocity across the rotor disk. The median moments at the channel bottom are nearly double the surface value, and the increase between the surface and the bottom is nearly linear. At mid-depths, the magnitude of M_z is similar to the magnitude of M_y. Much like M_y, the magnitude of the 90th percentile bending moments is approximately double the mean.

For M_z, waves again have the largest impact on the magnitude and vertical profile of the bending moment. In particular, increasing the wave strength (bottom row of Figure 4.13(b)) decreases the bending moments by 10-15% through the entire domain. Changes in wind shear

(Figure 4.14(a)) and stability (Figure 4.14(c)) result in minimal changes to the bending moment, while changes to the mean velocity (Figure 4.14(d)) again result in large changes to the magnitude of M_z.

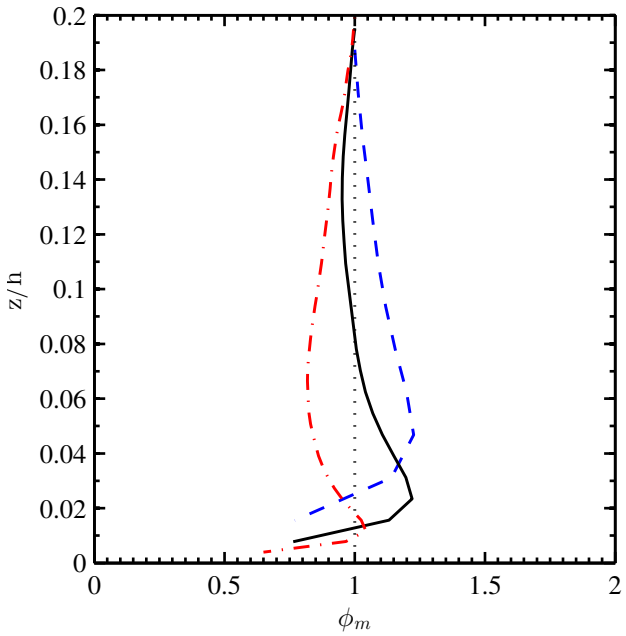

Figure 4.2: Vertical profiles of ϕ_m defined in (4.1) for three different grid resolutions, corresponding to the simulations B (solid black lines), B_- (blue dashed lines), and B_+ (red dash-dot lines), as a function of z/h.

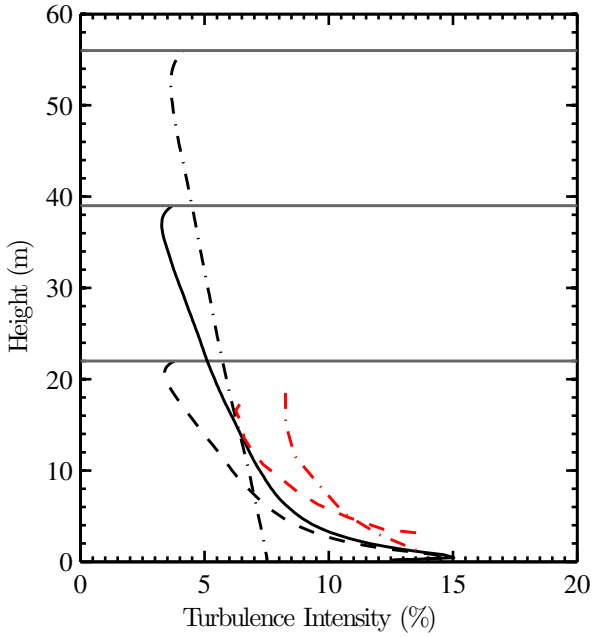

Figure 4.3: Turbulence intensity (TI) as a function of z/h for h =22m, 39m, and 56m, corresponding to simulations H_-, B, and H_+, respectively. Observational results from Thomson **et al.**[32] are also shown for the 22m Nodule Point location (red dashed line) and the 56m Admiralty Head location (red dash-dot line).

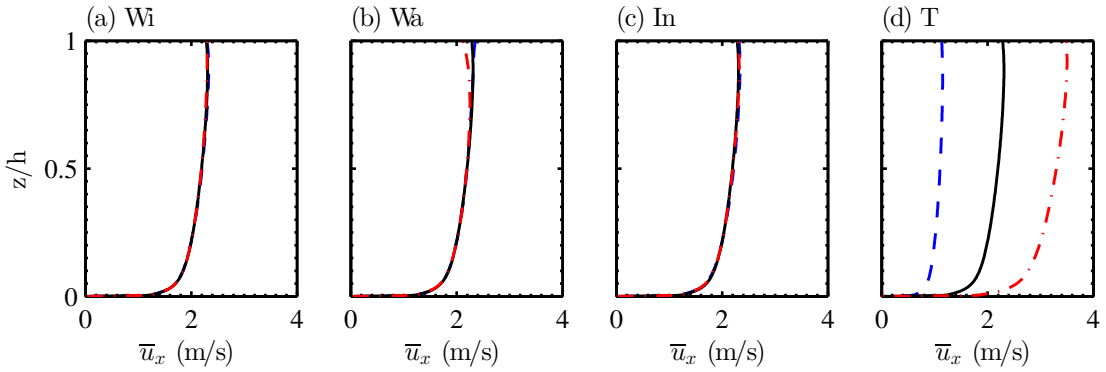

Figure 4.4: Vertical profiles of $\overline{u}_x$ for (a) $\mathrm{Wi}_{\pm}$, (b) $\mathrm{Wa}_{\pm}$, (c) $\mathrm{In}_{\pm}$, and (d) $\mathrm{T}_{\pm}$. Solid black lines are baseline results for case B, dashed blue lines show Wi_{-}, Wa_{-}, In_{-}, and T_{-}, and red dash-dot lines show Wi_{+}, Wa_{+}, In_{+}, and T_{+}.

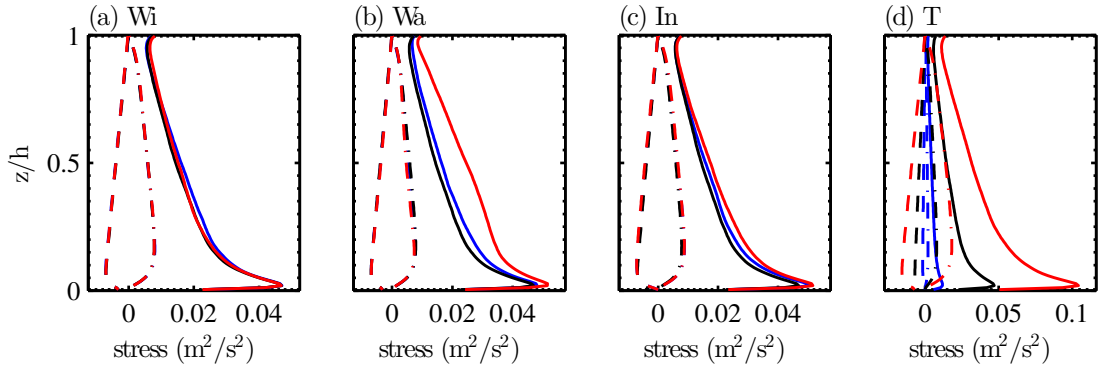

Figure 4.5: Vertical profiles of Reynolds stresses $\overline{u_x'^2}$ (solid), $\overline{u_x' u_z'}$ (dashed), and $\overline{u_z'^2}$ (dash-dot) for (a) $\mathrm{Wi}_{\pm}$, (b) $\mathrm{Wa}_{\pm}$, (c) $\mathrm{In}_{\pm}$, and (d) $\mathrm{T}_{\pm}$. Black lines are baseline results for case B, blue lines show Wi_{-}, Wa_{-}, In_{-}, and T_{-}, and red lines show Wi_{+}, Wa_{+}, In_{+}, and T_{+}.

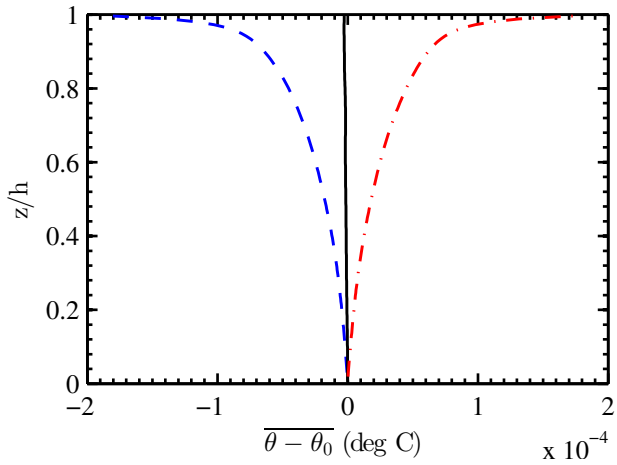

Figure 4.6: Vertical profiles of $\overline{\theta - \theta_0}$ for unstable In_{-} (blue dashed line), baseline B (black solid line), and stable In_{+} (red dash-dot line) simulations.

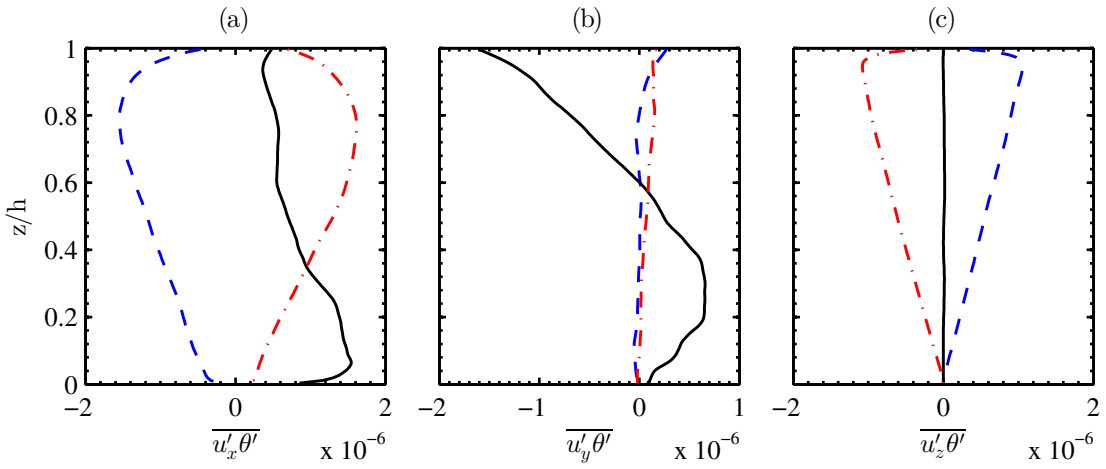

Figure 4.7: Vertical profiles of (a) $\overline{u'_x\theta'}$, (b) $\overline{u'_y\theta'}$, and (c) $\overline{u'_z\theta'}$ for In$_-$ (blue dashed lines), B (black solid lines), and In$_+$ (red dash-dot lines) simulations.

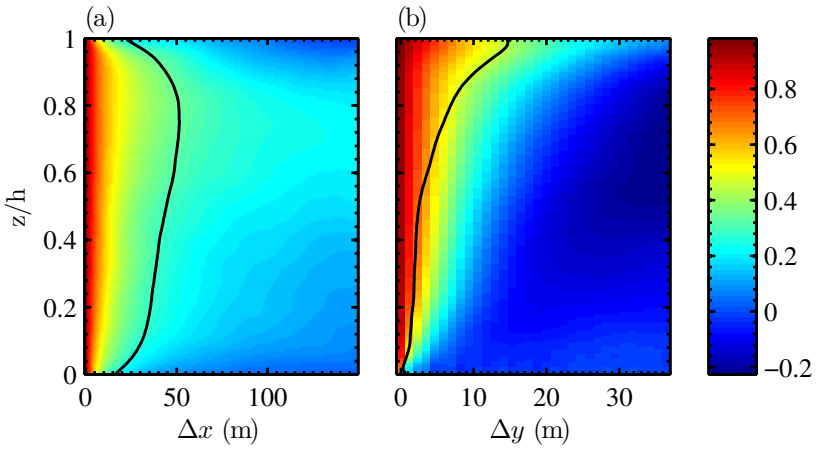

Figure 4.8: Vertical profiles of the (a) longitudinal, $f_{11}(z, \Delta x)$, and (b) transverse, $f_{12}(z, \Delta y)$, correlation functions for the baseline simulation (B). Solid black lines show the integral scales Λ_{11} and Λ_{12} defined in (4.4).

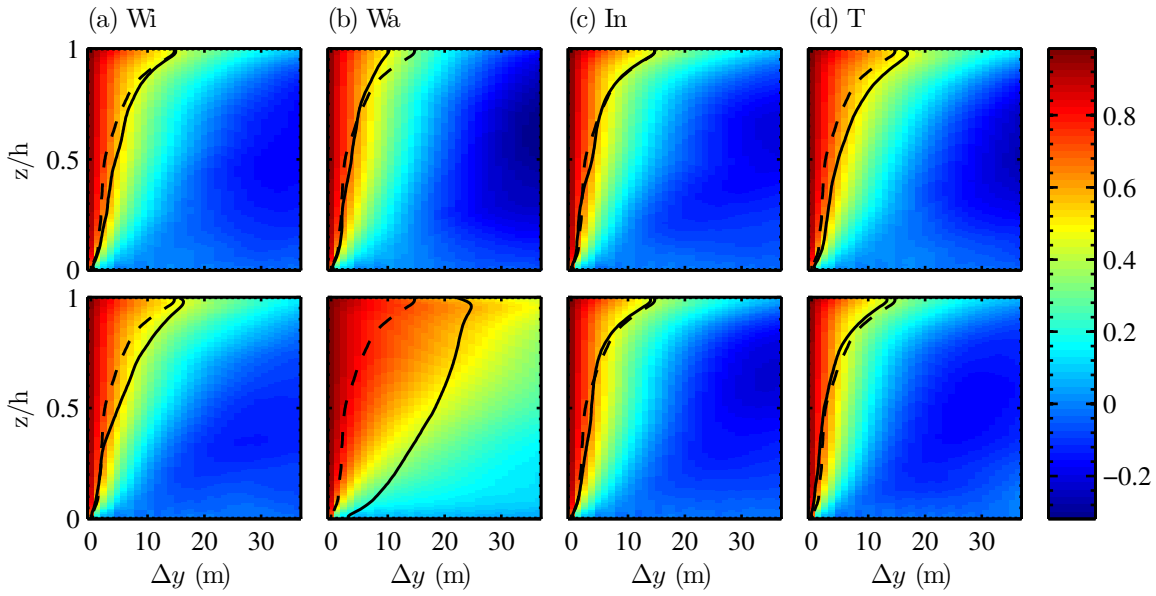

Figure 4.9: Vertical profiles of the transverse correlation $f_{12}(z, \Delta y)$ for (a) $\mathrm{Wi}_{\pm}$, (b) $\mathrm{Wa}_{\pm}$, (c) $\mathrm{In}_{\pm}$, and (d) $\mathrm{T}_{\pm}$. The top row shows Wi_{+}, Wa_{+}, In_{+}, and T_{+} and the bottom row shows Wi_{-}, Wa_{-}, In_{-}, and T_{-}. Solid black lines are Λ_{12} for each simulation and dashed black lines are Λ_{12} for the base case (B).

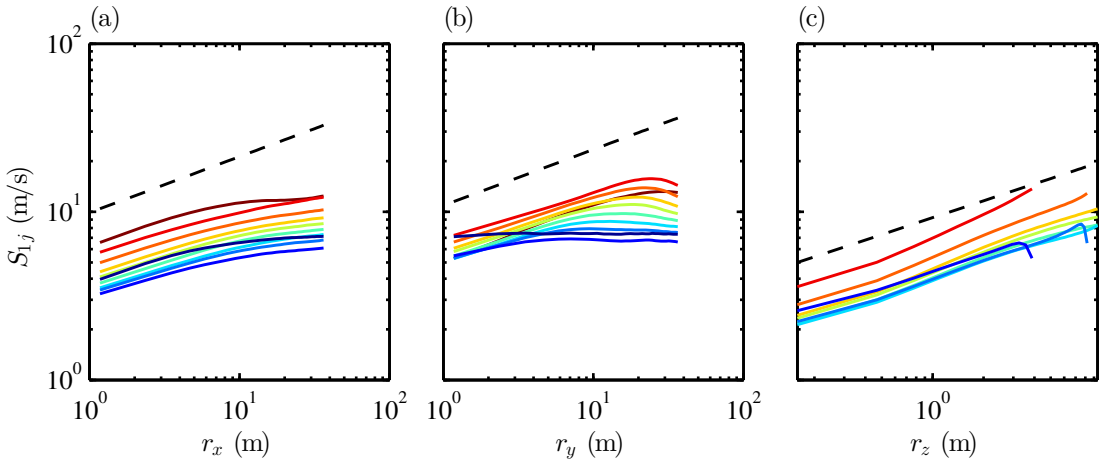

Figure 4.10: Structure functions (a) S_{11}, (b) S_{12}, and (c) S_{13} for the baseline simulation (B), where the structure functions are defined in (4.5). Various heights are shown, for z/h between 0 (blue) and 1 (red).

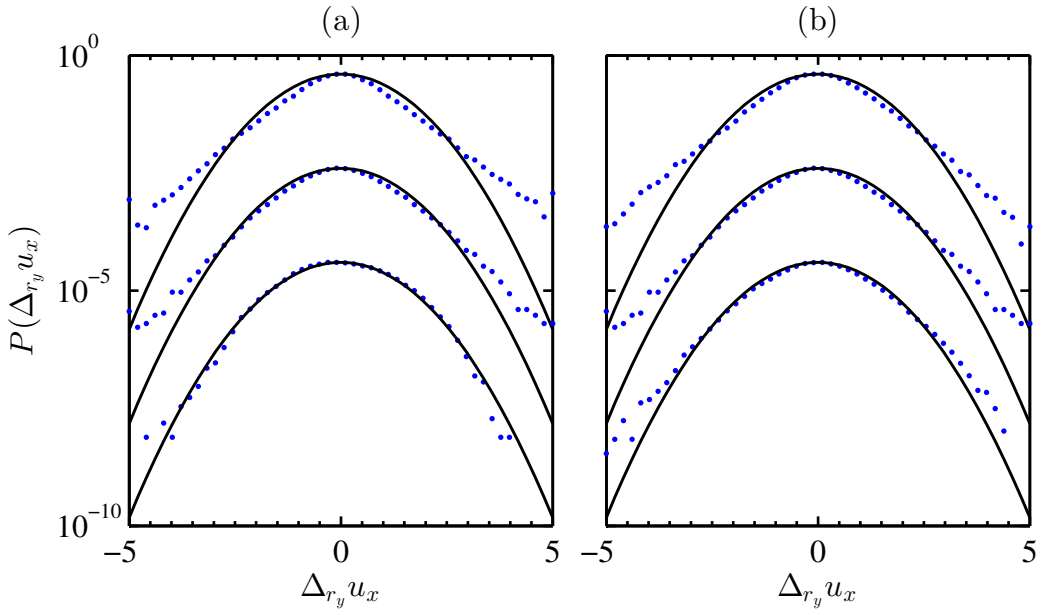

Figure 4.11: Pdfs $P(\Delta_{r_y} u_x)$ for (a) Δ_{r_y} =1, 5, and 25m at z =15m and (b) Δ_{r_y} =5m at z =5, 15, and 25m. Solid black lines show Gaussian distributions.

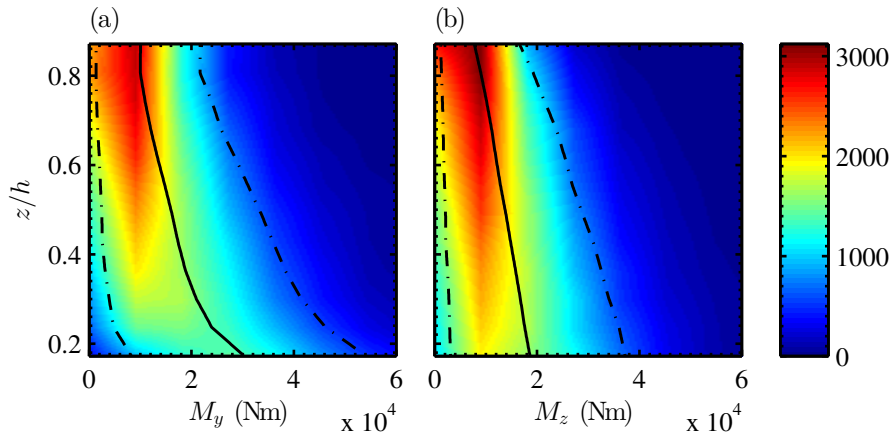

Figure 4.12: Bending moments (a) $M_y(z)$ and (b) $M_z(z)$ as functions of height z/h for the baseline simulation (B). The magnitude of the bending moment is represented by the color, the median bending moments are shown as solid black lines, and 10th and 90th percentiles are shown as black dash-dot lines.

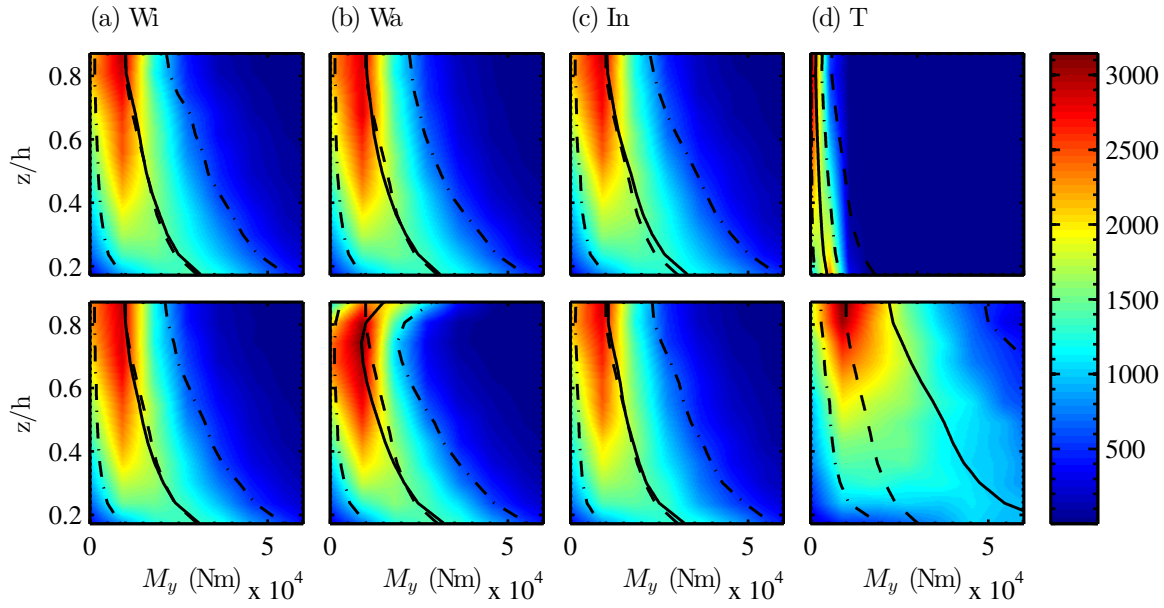

Figure 4.13: Shear-dominated bending moments M_y for (a) $\mathrm{Wi}_{\pm}$, (b) $\mathrm{Wa}_{\pm}$, (c) $\mathrm{In}_{\pm}$, and (d) $\mathrm{T}_{\pm}$. The top row shows Wi_{+}, Wa_{+}, In_{+}, and T_{+} and the bottom row shows Wi_{-}, Wa_{-}, In_{-}, and T_{-}. The median bending moments for each simulation case are shown as solid black lines, and 10th and 90th percentiles are shown as black dash-dot lines. Baseline results for the median moments are shown as black dashed lines.

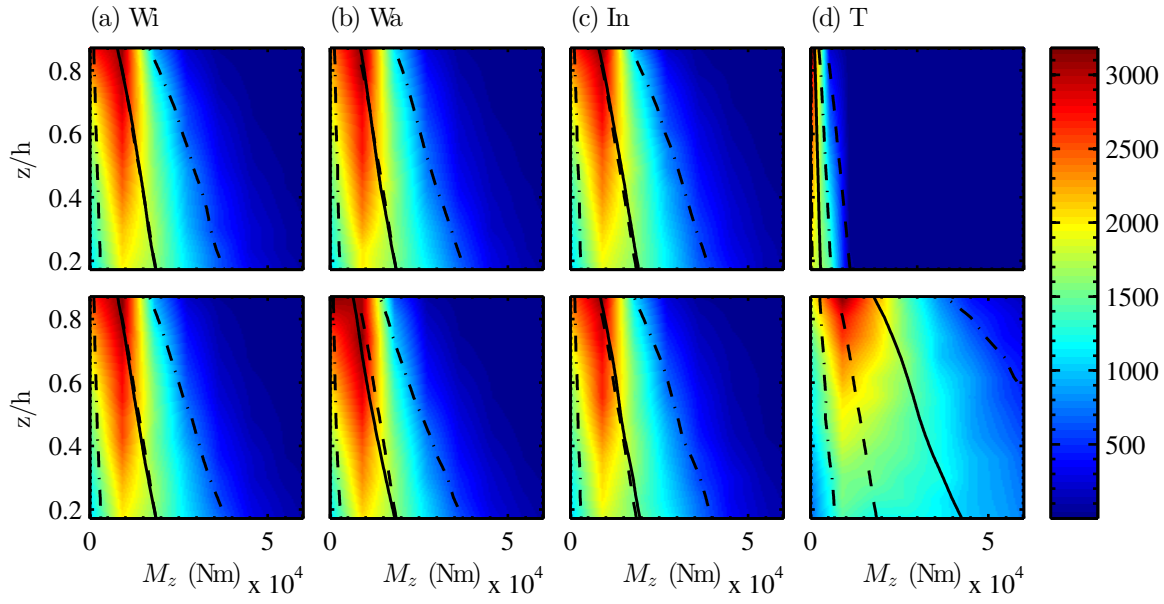

Figure 4.14: Eddy-dominated bending moments M_z for (a) $\mathrm{Wi}_{\pm}$, (b) $\mathrm{Wa}_{\pm}$, (c) $\mathrm{In}_{\pm}$, and (d) $\mathrm{T}_{\pm}$. The top row shows Wi_{+}, Wa_{+}, In_{+}, and T_{+} and the bottom row shows Wi_{-}, Wa_{-}, In_{-}, and T_{-}. The median bending moments for each simulation case are shown as solid black lines, and 10th and 90th percentiles are shown as black dash-dot lines. Baseline results for the median moments are shown as black dashed lines.

Chapter 5

Discussion

In Sections 2, 3, and 4, methodologies for simulating flows in ocean tidal channels have been outlined and results pertaining to loading of ocean current turbines in these environments have been presented. These methods and results have implications for turbine designers, observational campaign managers, and channel simulation designers; implications for each of three groups are outlined in more detail below.

5.1 Implications for Turbine Designers

Based upon the presented results, the most important consideration for a turbine designer should be the choice of hub height. Turbines mounted near the ocean floor not only see much larger bending moments (Figure 4.12), but also much lower velocities (Figure 4.4(a)), while turbines higher in the ocean boundary harness power from much higher velocity flows with lower magnitude bending loads. One of the main drivers of turbulence near the ocean surface – strong waves – have been shown to actually decrease the bending moment at moderate depths (Section 4.4); it should be noted, however, that this analysis only considers bending loads and not transient torque loads.

Effects of length scale and the structure function magnitude have also been shown to combine in interesting ways that warrant additional investigation by turbine designers. The inclusion of stronger waves in the simulation results in a large increase in the transverse length scale, which is a likely contributor to overall decreased bending moments at many depths for the strong wave simulation. Design flexibility in rotor diameter could allow for an opportunity to decrease overall

loads by ensuring rotor diameter is a different order of magnitude than the scale of the turbulent eddies.

Finally, turbine designers should keep in mind that the underlying drivers of bending moments have been shown to deviate from a normal distribution. Extreme loads will occur more frequently than a simple Gaussian distribution, which is fully characterized by its mean and standard deviation, would imply. Designers should account for these higher probabilities in assessing turbine loads.

5.2 Implications for Observational Campaigns

Observational campaigns are critical for understanding the specific environment in which a proposed turbine will be installed. These campaigns allow for very accurate understanding of mean velocities and the primary component of turbulence kinetic energy. Of all physical properties investigated in this paper, the mean tidal velocity has shown the largest impact on overall bending moment magnitude.

Through the analytical derivation (Section 2), loads have been shown to tie closely to two point correlations and structure functions. For these properties to be understood in a specific installation environment, two point measurements are needed – a single measurement device cannot capture the transverse length scales and structure functions. While capturing a variety of measurement widths and physical conditions will help understand bending loads, the present study indicates that priority should be given to capturing information on transverse lengths of the same scale as the turbine diameter and towards capturing diverse wave conditions.

Finally, as waves have been shown to have a very large impact on bending moments (Section 4.4), campaign managers should consider capturing wave specific data, such as amplitude and period, to accompany data on mean velocities and turbulence kinetic energy. These wave properties will help designers and modelers better understand the turbulence oceanic environment. Stability was found to be less important in understanding loads, though measurements of the temperature flux would still aid future simulations.

5.3 Implications for Ocean Channel Simulations

Ocean channel simulations have the potential to supplement and enhance measurement campaigns in the design process. However, for maximum effect, simulations should include physics most relevant to ocean current boundary conditions.

In the present analysis of bending moments, it was found that the most important variables to consider in the simulation process were mean tidal velocity and waves. Simulations should assess a variety of tidal velocities that are anticipated at the installation site, not just the mean velocity. Waves were found to be important, particularly in the top 70% of the boundary layer, and should be included in simulation physics.

One parameter that was found to have little effect on the resulting bending moments was stability. The present set of simulations use the Boussinesq hypothesis (as described in Section 3), but for estimating mean and 90th percentile loads, stability effects were negligible. However, this study has only investigated moderate levels of surface heating and cooling; for areas with more substantial heating and cooling effects, additional analysis is required.

Comparisons of the simulation results to the measurement campaigns from Thomson **et al.**[32], show that the simulations underestimate the turbulence intensity profile in the tidal channel. One possible explanation for this is the influence of distant bathymetry features on the free stream turbulence. In the case of a complex surrounding environment, free stream turbulence in the simulation may need to be supplemented to account for these non-local effects.

Finally, it was found in the simulations that high levels of grid anisotropy (the ratio of Δx to Δz) resulted in substantial deviations from a log-layer profile. While the ocean channel environment lends itself well to anisotropic grids – the horizontal domain length is typically much larger than the vertical – efforts should be made to either keep the grid anisotropy below four or to adapt the sub-grid scale model of a length scale to account for the grid anisotropy.

Chapter 6

Conclusions

A set of large eddy simulations were run to better understand the tidal channel environment and the unsteady loads and bending moments experienced by an ocean current turbine, with a focus on the physical parameters which impact these loads. The simulations were validated against past simulations as well as observational data from the Admiralty Head and Nodule Point inlets off the coast of Washington. The simulations were found to match both prior studies and observational data, although the simulations slightly underestimated the turbulence intensity profile.

In addition to simulation results and statistics, an analytical derivation was presented, linking turbulent statistics, namely $\Delta_{r_y} u'_x$ and $\Delta_{r_z} u'_x$, to bending moments. This derivation could provide a means of estimating the maximum bending moments from a limited set of observational data.

The simulations were analyzed to present information on mean velocity, Reynolds stresses, longitudinal and transverse correlations, length scales, structure functions and bending moment distributions. The vertical and horizontal bending moments were found to be of the same order of magnitude at moderate depths, though horizontal bending moments increased substantially near the ocean floor. The mean tidal velocity profile and wave strength were found to be the most important physical factors in determining the bending moment magnitude and distribution.

For future work, expanding the analysis to include statistics and distributions on transient torque loads is the primary task. The analysis could also be expanded to run the resulting simulation velocity snapshots through an advanced turbine simulator to provide statistics on all forms of turbine load. Additionally, comparisons against other observational campaigns could further vali-

date the simulation parameters while also providing guidance on any needed free stream turbulence supplements for different environment types.

Bibliography

[1] I. Afgan, J. McNaughton, S. Rolfo, D.D. Apsley, T. Stallard, and P. Stansby. Turbulent flow and loading on a tidal stream turbine by LES and RANS. Int. J. Heat Fluid Flow, 43:96–108, 2013.

[2] A.S. Bahaj, W.M.J. Batten, A.F. Molland, and J.R. Chaplin. Experimental investigation into the hydrodynamic performance of marine current turbines. Sust. Energy Ser. Report 3, 2005.

[3] A.S. Bahaj and L. Myers. Analytical estimates of the energy yield potential from the Alderney Race (channel islands) using marine current energy converters. Renewable Energy, 29(12):1931–1945, 2004.

[4] M. Calaf, C. Meneveau, and J. Meyers. Large eddy simulation study of fully developed wind-turbine array boundary layers. Physics of Fluids, 22(015110), 2010.

[5] Leonardo P. Chamorro and Fernando Porté-Agel. A wind-tunnel investigation of wind-turbine wakes: Boundary-layer turbulence effects. Boundary-Layer Meteorology, 132(1):129–149, 2009.

[6] M. J Churchfield, Y. Li, and P. J Moriarty. Large-eddy simulation study of wake propagation and power production in an array of tidal-current turbines: Preprint. July 2011.

[7] Matthew J. Churchfield, Sang Lee, Patrick J. Moriarty, Luis A. Martinez, Stefano Leonardi, Ganesh Vijayakumar, and James G. Brasseur. A large-eddy simulation of wind-plant aerodynamics. AIAA Paper 2012-537, 2012.

[8] MA Donelan, J Hamilton, and WH Hui. Directional spectra of wind-generated waves. Philosophical Transactions of the Royal Society of London Series A-Mathematical Physical and Engineering Sciences, 315(1534):509–562, 1985.

[9] P. E. Hamlington, L. P. Van Roekel, B. Fox-Kemper, K. Julien, and G. P. Chini. Langmuir-Submesoscale Interactions: Descriptive Analysis of Multiscale Frontal Spin-down Simulations. Submitted to Journal of Physical Oceanography., 2014.

[10] B.J. Jonkman and L. Kilcher. TurbSim User's Guide: Version 1.06.00. Technical Report TP-xxx-xxxx, NREL, 2012.

[11] Jason M. Jonkman and Marshall L. Buhl Jr. FAST User's Guide. Golden, CO: National Renewable Energy Laboratory, 2005.

[12] Seokkoo Kang, Iman Borazjani, Jonathan A. Colby, and Fotis Sotiropoulos. Numerical simulation of 3D flow past a real-life marine hydrokinetic turbine. Advances in Water Resources, 39:33–43, 2012.

[13] Seokkoo Kang, Anne Lightbody, Craig Hill, and Fotis Sotiropoulos. High-resolution numerical simulation of turbulence in natural waterways. Advances in Water Resources, 34(1):98–113, 2011.

[14] N. D. Kelley, B. J. Jonkman, G. N. Scott, J. T. Bialasiewicz, and L. S. Redmond. The impact of coherent turbulence on wind turbine aeroelastic response and its simulation. In Windpower 2005 Conference Proceedings, 2005.

[15] Jason H. Laks, Lucy Y. Pao, and Alan D. Wright. Control of wind turbines: Past, present, and future. In American Control Conference, 2009. ACC'09., pages 2096–2103, 2009.

[16] I Langmuir. Surface motion of water induced by wind. Science, 87:119–123, 1938.

[17] Adam W. Lavely, Ganesh Vijayakumar, James G. Brasseur, Eric G. Paterson, and Michael P. Kinzel. Comparing unsteady loadings on wind turbines using TurbSim and LES flow fields. 2012.

[18] M. Li, S. Radhakrishnan, U. Piomelli, and W. Rockwell Geyer. Largeeddy simulation of the tidalcycle variations of an estuarine boundary layer. Journal of Geophysical Research, 115(C08003), 2010.

[19] R. Malki, A.J. Williams, T.N. Croft, M. Togneri, and I. Masters. A coupled blade element momentum-computational fluid dynamics model for evaluating tidal stream turbine performance. Applied Mathematical Modelling, 37:3006–3020, 2013.

[20] K. McCaffrey, B. Fox-Kemper, P. E. Hamlington, and J. Thomson. Characterization of Turbulence Anisotropy, Coherence, and Intermittency at a Prospective Tidal Energy Site: Observational Data Analysis. Submitted to Renewable Energy., 2014.

[21] R. McSherry, J. Grimwade, I. Jones, S. Mathias, A. Wells, and A. Mateus. 3D CFD modelling of tidal turbine performance with validation against laboratory experiments. In Proc. 9th European Wave and Tidal Energy Conference, University of Southampton, UK, 2011.

[22] J. C. McWilliams, P. P. Sullivan, and C. H. Moeng. Langmuir turbulence in the ocean. Journal of Fluid Mechanics, 334(1):1–30, 1997.

[23] Johan Meyers and Charles Meneveau. Large eddy simulations of large wind-turbine arrays in the atmospheric boundary layer. AIAA Paper 2010-827, 2010.

[24] Johan Meyers and Charles Meneveau. Flow visualization using momentum and energy transport tubes and applications to turbulent flow in wind farms. arXiv preprint arXiv:1209.4578, 2012.

[25] Chin-Hoh Moeng. A large-eddy-simulation model for the study of planetary boundary-layer turbulence. Journal of the Atmospheric Sciences, 41(13):2052–2062, 1984.

[26] L. Myers and A. S. Bahaj. Near wake properties of horizontal axis marine current turbines. In Proceedings of the 8th European Wave and Tidal Energy Conference, pages 558–565, 2009.

[27] L. Myers and A.S. Bahaj. Simulated electrical power potential harnessed by marine current turbine arrays in the Alderney Race. Renewable Energy, 30(11):1713–1731, 2005.

[28] Lucy Y. Pao and Kathryn E. Johnson. A tutorial on the dynamics and control of wind turbines and wind farms. In American Control Conference, 2009. ACC'09., pages 2076–2089, 2009.

[29] F. Porté-Agel, Y.-T. Wu, H. Lu, and L. Chamorro. Large-eddy simulation of wind-turbine wakes: Evaluation of turbine parameterizations. In 10th EMS Annual Meeting, 10th European Conference on Applications of Meteorology (ECAM) Abstracts, held Sept. 13-17, 2010 in Zürich, Switzerland. http://meetings.copernicus.org/ems2010/, id.EMS2010-606, volume -1, page 606, September 2010.

[30] Peter P. Sullivan, James C. McWilliams, and Chin-Hoh Moeng. A subgrid-scale model for large-eddy simulation of planetary boundary-layer flows. Boundary-Layer Meteorology, 71(3):247–276, 1994.

[31] Peter P. Sullivan and Edward G. Patton. The effect of mesh resolution on convective boundary layer statistics and structures generated by large-eddy simulation. Journal of the Atmospheric Sciences, 68(10), 2011.

[32] J. Thomson, B. Polagye, V. Durgesh, and M.C. Richmond. Measurements of turbulence at two tidal energy sites in Puget Sound, WA. IEEE Journal of Oceanic Engineering, 37(3):363–374, 2012.

[33] U.S. Department of Energy. Ocean energy technology overview. 2009.

[34] L. P. Van Roekel, B. Fox-Kemper, P. P. Sullivan, P. E. Hamlington, and S. R. Haney. The form and orientation of Langmuir cells for misaligned winds and waves. Journal of Geophysical Research-Oceans, 117:C05001, 2012.

[35] A. Webb, Baylor Fox-Kemper, E. Baldwin-Stevens, G. Danabasoglu, B. Hamlington, W.G. Large, and S. Peacock. Global climate model sensitivity to estimated Langmuir mixing. Ocean Modelling, page in preparation, 2012.